Experimental study of sheathed cold-formed steel beam-columns

Constantinos Kyprianou*, Pinelopi Kyvelou, Leroy Gardner, David A. Nethercot

Department of Civil and Environmental Engineering, Imperial College London, South Kensington Campus, London SW7 2AZ, UK

Abstract

An experimental study of sheathed cold-formed steel C-lipped wall studs, with service holes, subjected to compression and major axis bending is presented in this paper. A total of 17 experiments were performed with both oriented strand board (OSB) and plasterboard used as sheathing and with varying connector spacing employed between the sheathing panels and the steel members. The tested specimens comprised a single 2.4 m long column sheathed on both sides and secured at the ends to top and bottom tracks. The member tests were complemented by material tests, stub column tests and initial geometric imperfection measurements. The specimens were tested in a dual-actuator rig where axial compression was applied by means of a vertical actuator through the top track, while bending was applied through the application of four lateral point loads. Eight pure compression tests with both plasterboard and OSB sheathing and with the spacing of the connectors varying between 75 mm and 600 mm were initially performed. Specimens with OSB sheathing were then tested under pure bending and combined loading. The full load-deformation responses and failure modes of the member test specimens are reported. The compressed studs connected to the plasterboard sheathing at wider spacings exhibited pull-through failure of the connectors, followed by flexural torsional buckling, while the specimens with denser connector spacings, failed by local buckling at the member ends. The OSB sheathed specimens under pure compression failed by local and distortional buckling, those under combined loading exhibited local failure at the service openings, while for those under pure bending, local buckling and stud-to-track connector failure occurred. Reducing the spacing of the connectors from 600 mm to 75 mm resulted in up to 20% and 30% increases in capacity

for the studs sheathed with OSB and plasterboard respectively.

Keywords: experiments, cold-formed steel, plasterboard, OSB, sheathing, testing

1. Introduction

Wall systems made from cold-formed steel C-lipped vertical members (studs) set in tracks and sheathed with wood-based boards or gypsum plasterboards are becoming increasingly common in the construction industry. The versatility, practicality and economy associated with the quick construction process of these systems allows for their use both as non-structural and load-bearing wall systems. When used as load bearing systems, additional cold-formed steel members are employed to provide lateral bracing, as illustrated in Figure 1 (a), although several studies [1, 2] have shown that the attached sheathing (Figure 1 (b)) can provide sufficient bracing and result in improved axial and flexural capacities.

Increased compression capacities for cold-formed steel columns, achieved due to their connection with sheathing, have been experimentally demonstrated in various studies [3–9]. Studies on gypsum-sheathed stud-members subjected to major axis bending [10] have highlighted that, if pull-through fastener failures are prevented, significant enhancements in load-bearing capacity can be achieved. Observed enhancements in load-bearing capacity with decreasing connector spacing between the sheathing and the steel [6, 10, 11] are believed to arise due to greater restraining effects and the mobilisation of composite action between the two materials.

Wall stud under combined compression and major axis bending, which can be the result of gravity and wind actions have received limited study. Single-sided OSB sheathed studs and double-sided sheathed studs with OSB and gypsum boards under various combinations of compression and bending, were examined and compared against results from bare steel studs in [11].

*Corresponding author

Email addresses: constantinos.kyprianou08@imperial.ac.uk (Constantinos Kyprianou, pinelopi.kyvelou11@imperial.ac.uk (Pinelopi Kyvelou), leroy.gardner@imperial.ac.uk (Leroy Gardner), d.nethercot@imperial.ac.uk (David A. Nethercot)

The focus of the experimental study presented herein is to extend the existing experimental data and demonstrate that using closer-spaced connectors between the column and the sheathing can further enhance the capacity of stud-wall systems under both compression and bending, as well as preventing sudden failure of the sheathing-to-steel connectors. Sheathed stud columns, representative of a single vertical element in a stud wall system [1, 2], are tested under combined compression and bending – see Figure 1 (c). Note that the tested members also featured service holes, as shown in Figure 2. The material and geometric properties of all system components are provided in Section 2, while imperfection measurements, along with a detailed description of the specimens and of the test rig are reported in Section 3. The obtained results are presented in Section 4 with a discussion following in Section 5.

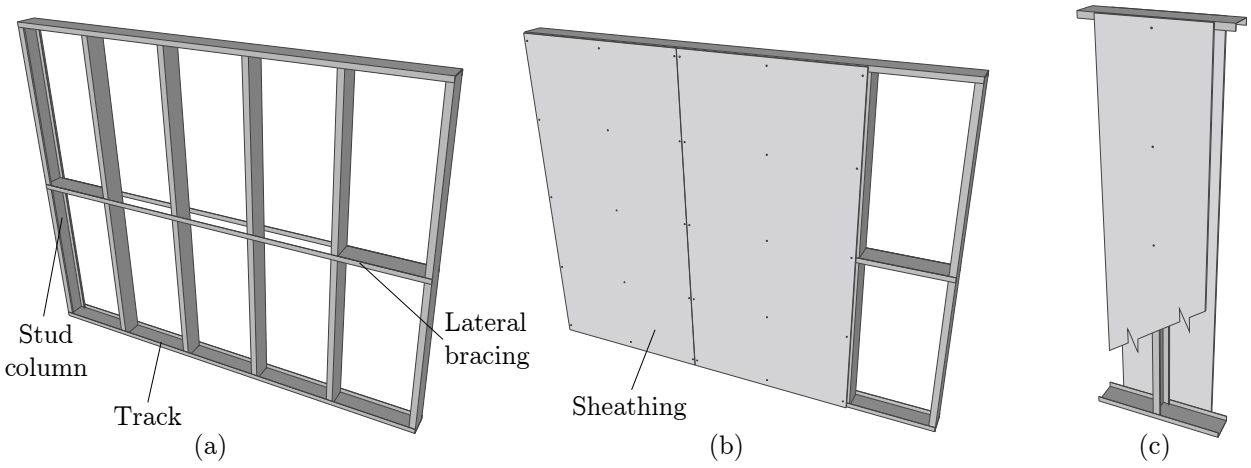

Figure 1: Illustrations of (a) stud wall with lateral bracing (b) stud wall with sheathing (c) single sheathed column

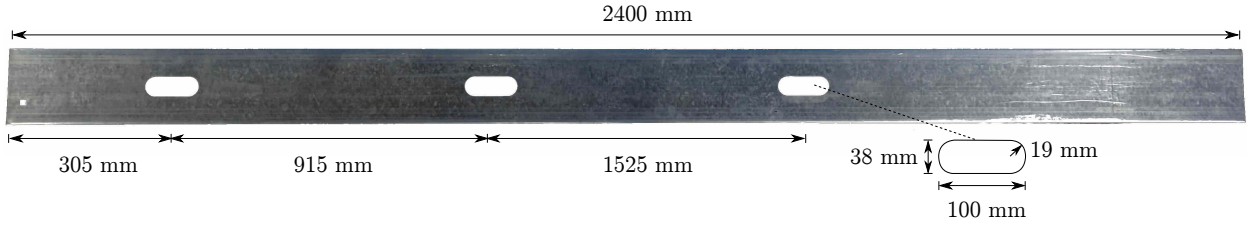

Figure 2: Stud column test specimen showing arrangement of service openings

2. Material tests

The stress-strain behaviour and key materials properties of the main components of the examined sheathed stud columns, shown in Figure 1 (c), were determined by coupon testing, as described in this section.

2.1. Cold-formed steel

For the determination of the material properties of the steel stud and track of steel grade S450GD (galvinised with zinc coat Z275) [12, 13], three coupons were extracted along the length of the web of both members. The notation of the coupons begins with the letters CS, followed by the nominal thickness in mm multiplied by 10 (i.e. CS15 for the studs and CS12 for the track) and then the test number. The tensile coupons were tested in accordance with EN ISO 6892 [14] at an initial axial strain rate of 0.00007 s^{-1} which was gradually increased to 0.00025 s^{-1} via three intermediate steps. A 150 kN Instron 5984 testing machine was used to perform the tests, along with the Bluehill data acquisition system, collecting data every second. Accurate measurements of strains at the early stages of loading was ensured through the use of two strain gauges, mounted at mid-height on either side of the coupons, while an optical extensometer with a gauge length of 50 mm was used as an additional strain measurement method to capture the later parts of the stress-strain curves.

The key measured properties are presented in Tables 1 and 2 while the full stress-strain curves are illustrated in Figures 3 (a) and (b) for the stud and track respectively. In Tables 1 and 2, E is the Young's modulus, $\sigma_{0.2}$ is the 0.2% proof stress (considered as the yield strength), $\sigma_{1.0}$ is the 1% proof stress, σ_u is the ultimate strength, ε_u is the strain at σ_u and ε_f is the elongation at fracture measured over the standard gauge length [14].

Table 1: Material properties of cold-formed steel coupons extracted from columns (CS15)

Designation	E (GPa)	$\sigma_{0.2}$ (MPa)	$\sigma_{1.0}$ (MPa)	σ_u (MPa)	ε_u	ε_f
CS15-1	203	481	481	514	0.069	0.121
CS15-2	203	484	484	514	0.089	0.148
CS15-3	205	481	482	514	0.079	0.120
Average	204	482	482	514	0.079	0.130

Table 2: Material properties of cold-formed steel coupons extracted from tracks (CS12)

Designation	E (GPa)	$\sigma_{0.2}$ (MPa)	$\sigma_{1.0}$ (MPa)	σ_u (MPa)	ε_u	ε_f
CS12-1	201	483	494	613	0.137	0.222
CS12-2	201	483	495	609	0.124	0.195
CS12-3	201	484	496	618	0.140	0.229
Average	201	483	495	613	0.134	0.215

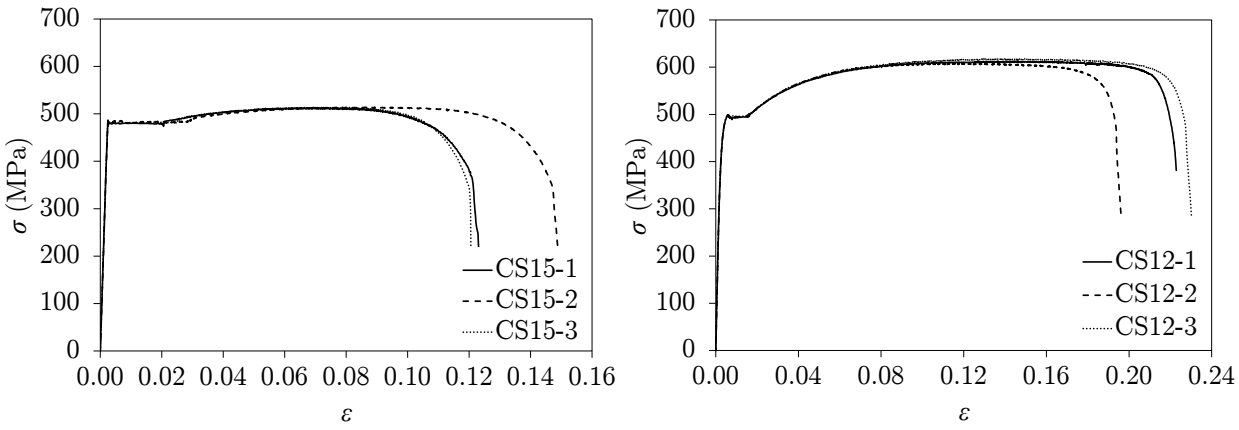

(a) CS15 - column

(b) CS12 - track

Figure 3: Stress-strain curves of tensile coupons extracted from (a) stud and (b) track

2.2. Sheathing material tests

Two types of sheathing board were used: standard gypsum-based plasterboards and orientated strand board. The employed plasterboard was type A board in accordance with

EN 520 [15], was of 12.5 mm measured thickness and 665 kg/m^3 density. The employed oriented strand board was type 3 (OSB/3) as specified in EN 300 [16], had a measured thickness of 11.0 mm and had a density of 590 kg/m^3. Material tests for both types of board were carried out in both compression and tension, as well as longitudinally and transversely to their direction of production in accordance with EN 789 [17]. A detailed description of these tests is provided in [18] while a summary of the key material properties is provided in Table 3, where E is the Young's modulus, f_u is the ultimate strength, ε_u is the corresponding strain and $\varepsilon_{u,0.8}$ (only for compression) is the strain at 80% of f_u, post f_u.

Table 3: Average measured material properties of sheathing

Type	Longitudinal				Transverse			
	E (GPa)	f_u (MPa)	ε_u (%)	$\varepsilon_{u,0.8}$ (%)	E (GPa)	f_u (MPa)	ε_u (%)	$\varepsilon_{u,0.8}$ (%)
OSB, tension	4.10	11.7	0.37	-	2.94	7.01	0.37	-
OSB, compression	4.02	12.1	0.40	0.54	2.78	10.7	0.50	0.66
Plasterboard, tension	1.65	1.45	0.61	-	1.67	0.67	0.38	-
Plasterboard, compression	2.11	3.81	0.23	0.37	2.13	3.33	0.23	0.42

3. Member tests

3.1. Geometric properties

The cross-sectional shape of the stud columns, which are the main structural members of the examined system, is illustrated in Figure 4 along with the notation used for the cross-sectional dimensions. The average measured dimensions of the stud columns and tracks (which do not feature a lip) are provided in Table 4, where t is the thickness, h is the depth of the section, b is the flange width, c is the length of the lip and r is the internal corner radius of the section.

All stud columns were 2.4 m long and positioned in the centre of 800 mm long tracks. The columns came with 100×38 mm pre-cut holes for the installation of services, which is typical for columns deeper than 150 mm. The shape of the oval service holes, which had 19 mm radii at the ends, as well as their position along the column length are illustrated in Figure 2.

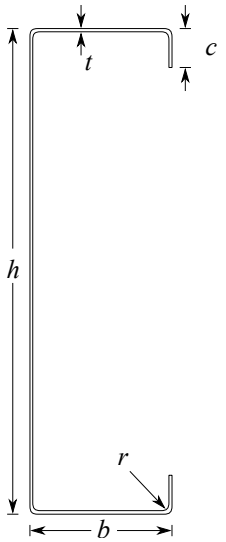

Figure 4: Notation for cross-sectional geometry of stud

Table 4: Average measured cross-sectional dimensions

Member	t (mm)	h (mm)	b (mm)	c (mm)	r (mm)
Column	1.44	149.15	43.92	11.95	2.50
Track	1.18	155.30	31.18	-	2.25

3.2. Stub column tests

A pair of stub columns were tested – one with and one without service hole openings in the web – to investigate the effect of the hole on the ultimate compression capacity of the section. Both columns were 450 mm long with the position of the hole for the respective member being at mid-length. The tests were carried out in accordance with EN 1993-1-3 [19], with the axial load introduced using a 750 kN Instron hydraulic testing machine at a constant displacement rate of 0.25 mm/min. Both tests were continued beyond the ultimate capacities to observe the post-peak behaviour and the development of the failure mechanism.

The obtained axial load-displacement curves along with images of the deformed test specimens are provided in Figure 5 (a) and (b) respectively. For both stub columns, failure was triggered by a combination of local and distortional buckling, with the specimen comprising a service hole exhibiting 5% reduced capacity compared to the one without a hole.

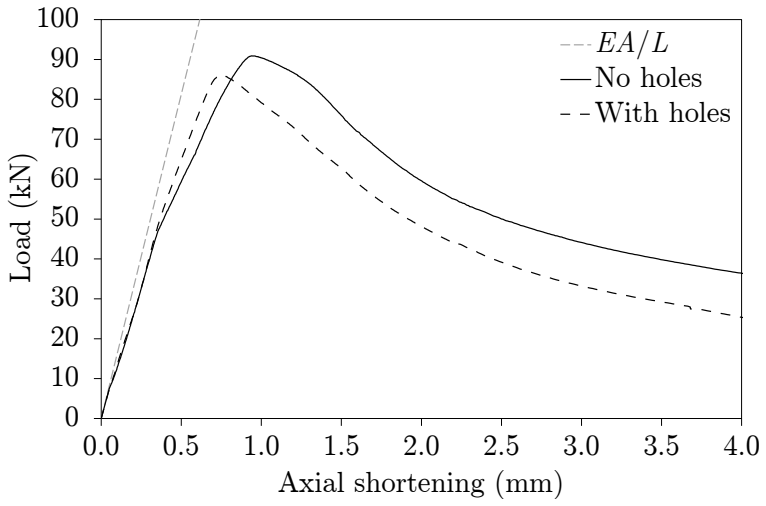

(a)

(b)

Figure 5: Stub column test results: (a) load-displacement curves and (b) failure modes

3.3. Imperfections

Initial geometric imperfections, including both cross-sectional (δ_L for local, δ_D for distortional) and global ($\delta_{G,maj}$ and $\delta_{G,min}$ for flexural about the major and minor axis respectively and $\theta_{G,t}$ for torsional) modes along the length of the member, were measured for ten specimens with service holes (- see Figure 2) and ten without service holes. The five modes of imperfection (the associated buckling modes of which are observed in Section 4), illustrated in Figure 6, were determined using an imperfection rig with seven LVDTs – see Figure 7 – which allowed the measurement of the variation of the cross-sectional shape along the length of the specimens. The method used to determine the imperfection magnitudes was similar to that described in [7]. The seven LVDT mount ran on rails, as shown in Figure 8, with an attached string pot allowing determination of the position of the measurements along the length of the column and with the rails calibrated to remove their inherent imperfection. Data were recorded using the acquisition system DATASCAN [20] every second.

The imperfections along the length of the columns were calculated using the following equations, where δ_L, δ_D, $\delta_{G,maj}$, $\delta_{G,min}$ and $\theta_{G,t}$ are as defined in Figure 6 and $\delta_1 - \delta_7$ are

the measurements of the LVDTs shown in Figure 7.

$$\delta_L = \text{mean}\left[(\delta_4 - \delta_3), (\delta_4 - \delta_5)\right] \quad (1)$$

$$\delta_D = \text{mean}\left[(\delta_1 - \delta_2), (\delta_7 - \delta_6)\right] \quad (2)$$

$$\delta_{G,maj} = \text{mean}\left[\delta_2, \delta_6\right] \quad (3)$$

$$\delta_{G,min} = \text{mean}\left[\delta_3, \delta_5\right] \quad (4)$$

$$\theta_{G,t} = (\delta_3 - \delta_5)/h \quad (5)$$

The average imperfection amplitudes of the specimens with and without service holes are provided in Table 5, relative to the thickness for the cross-sectional modes and relative to the column length L for the global modes. Typical distributions of the imperfections along the member length are presented in Figures 9 and 10 for the cross-sectional and global imperfections respectively. In Figure 9, all data have been post-processed such that the measurements are plotted relative to a best fit line through the overall imperfection profile. The imperfection amplitude for the cross-section modes is then taken as the maximum deviation from this line. This measure of imperfection is deemed to be appropriate because it is the deviation from flatness that is the key trigger and influential factor for local and distortional buckling. For the global imperfections, a half-sine wave was fitted to the measured curves using least squares regression to allow determination of the maximum amplitude at mid-length, as shown in Figure 10.

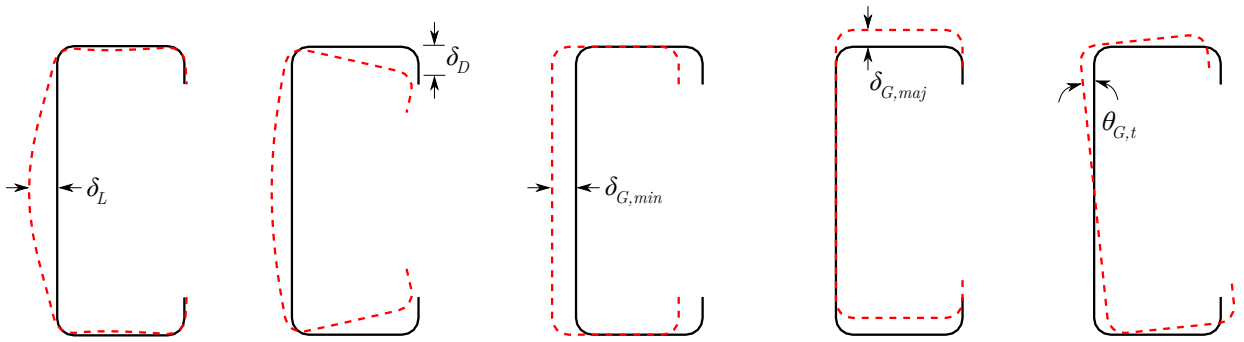

(a) Local (b) Distortional (c) Minor flexural (d) Major flexural (e) Torsional

Figure 6: Illustrations of amplitudes of imperfection shapes for (a) local, (b) distortional, (c) flexural about the minor axis, (d) flexural about the major axis and (e) torsional modes

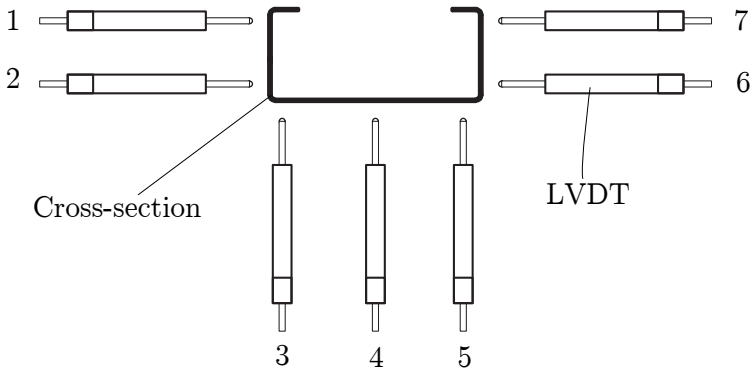

Figure 7: Positions of LVDTs mounted on the imperfection rig

(a) (b) (c)

Figure 8: Imperfection rig (a) elevation view (b) schematic and (c) detail of the rails and the LVDTs around the cross-section

Table 5: Summary of initial geometric imperfection amplitude measurements

Member		δ_L/t	δ_D/t	$L/\delta_{G,min}$	$L/\delta_{G,maj}$	$\theta_{G,t}$ (deg/m)
No holes	Mean	0.23	0.44	-1770	13000	0.19
	COV	0.19	0.22	0.23	0.36	0.24
With holes	Mean	0.21	0.52	4380	17700	0.15
	COV	0.16	0.19	0.35	0.47	0.20

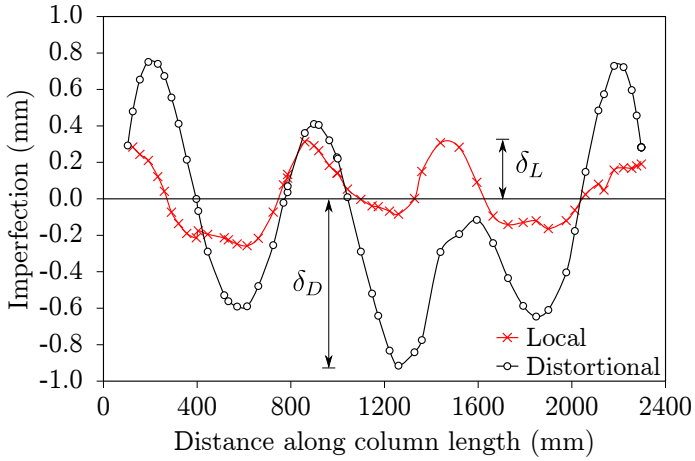

Figure 9: Cross-sectional imperfections along column length

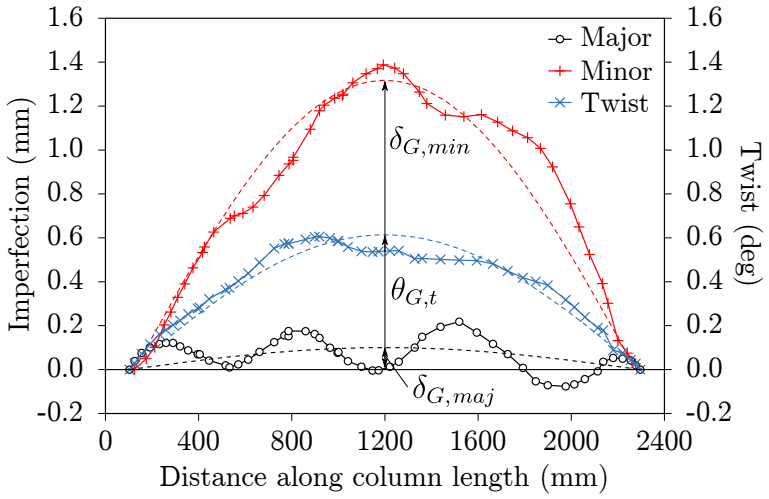

Figure 10: Global imperfections along the column length, with dashed lines marking the half-sine curves of best fit

The measured imperfection amplitudes for the members with and without holes show no significant discrepancies for the local, distortional, torsional and global major axis flexural modes, with the latter being around L/10000. Conversely, both the magnitude and direction of the minor axis bow imperfections were affected by the presence of the holes; this is attributed to the influence of the hole punching process. Note that the positive imperfection values denote that the imperfection direction is as per the illustration in Figure 6 (c), while negative values indicate that the imperfection direction is of the opposite sense.

3.4. Screws types and arrangements

The types of connector used for securing the sheathing panels to the steel studs were screws of 3.5 mm diameter for the plasterboard and 4.8 mm diameter for the OSB. Illustrations of the two screws are provided in Figure 11 (a) and (b) respectively, while further details of the properties of these screws and on their behaviour in shear and pull-through can be found in [18]. The connection between the flanges of the track and stud at both column ends were made using screws of 4.8 mm diameter - see Figure 11 (c). Finally, the webs of both tracks were secured onto square hollow sections, using bolts of 6 mm diameter (see Figure 11 (d)).

Figure 11: Types of connector used: (a) 3.5 mm diameter screw for plasterboard to steel (b) 4.8 mm diameter screw for OSB-to-steel (c) 4.8 mm diameter screw for steel-to-steel and (d) 6 mm diameter anchor bolt

The sheathed column specimens were tested with four different screw spacings: 600 mm, 300 mm, 150 mm and 75 mm, as shown in Figure 12. Note that a distance of 50 mm was kept between the edge connector and the column end, in order for the screw to not be driven

into the track. For the specimens with a spacing of 600 mm, five screws were used on each side of the column, with the two outer screw spacings reduced to 550 mm. Similarly, for the other arrangements, the outer spacings were reduced to allow for a uniform spacing of connectors along the rest of the column length. For the 300 mm spacing, nine screws were used, while for the 150 mm and the 75 mm spacings, 17 and 33 screws were employed respectively. No connection between the track and the sheathing was implemented since the focus of this study was to investigate the column-to-sheathing connection.

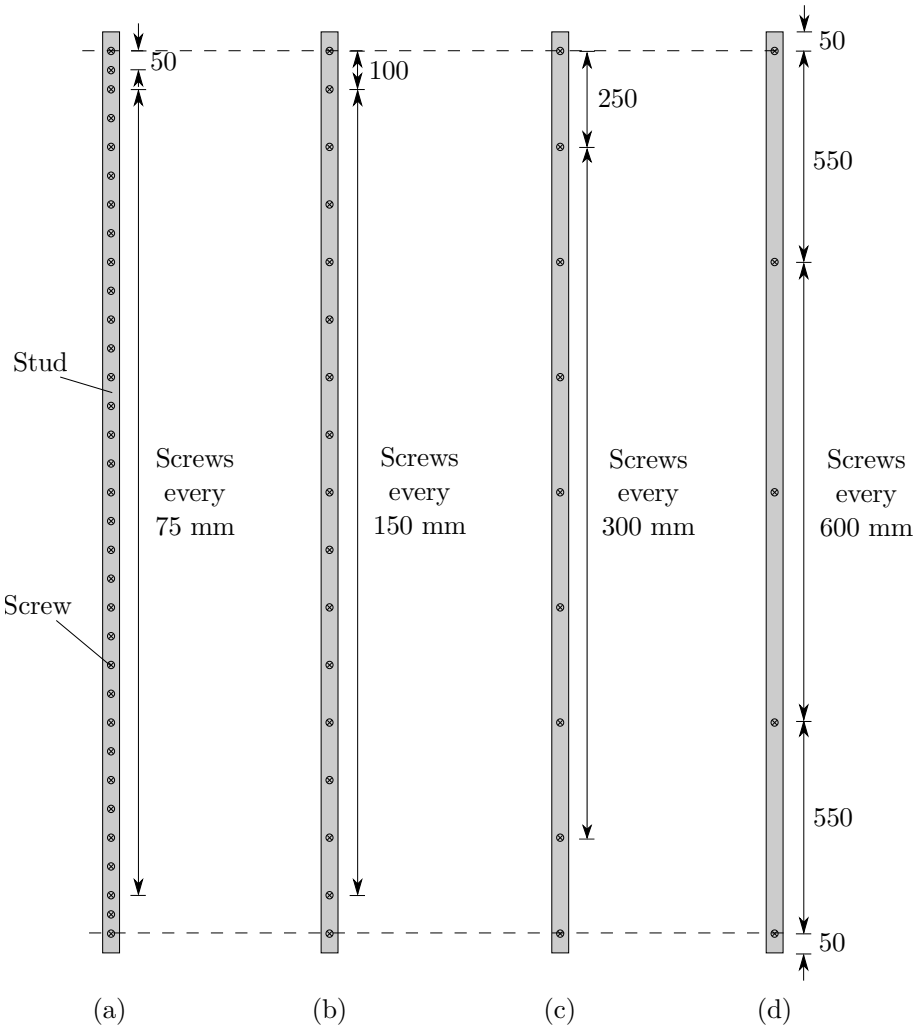

Figure 12: Connector arrangements for spacings of (a) 75 mm, (b) 150 mm, (c) 300 mm and (d) 600mm (dimensions in mm)

3.5. Test rig

The specimens were tested in a dual-actuator rig. Axial compression was applied to the overhead track by a vertical 1000 kN Instron actuator while bending was applied by laterally loading the sheathing using a four-line two-tier whiffletree system connected to an horizontal 500 kN Instron actuator in order to approximate a uniformly distributed load - see Figure 13. The top actuator was connected to a hot-rolled steel square hollow section, through which load was applied to the top track of the test specimens. Note that special attention was given to avoid contact between the square hollow section and the sheathing such that axial load would be applied directly to the steel stud only. Rotation of the hollow section was prevented by the use of brackets at either end (see Figure 13), while Teflon was placed between the brackets and the hollow section to minimise friction. The bottom track was also secured to a hollow section fixed to the concrete lab floor. The whiffletree connected to the horizontal actuator was free to rotate, with pinned connections between its legs. Prior to each test, the whiffletree was laser-aligned to be parallel to the column length.

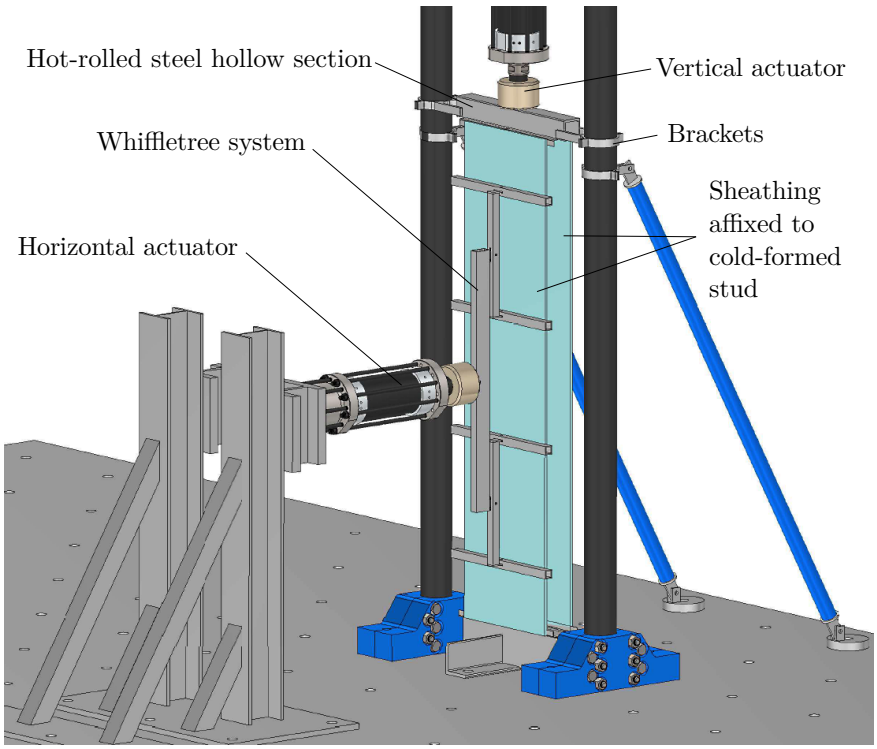

Figure 13: Illustration of rig for beam-column tests

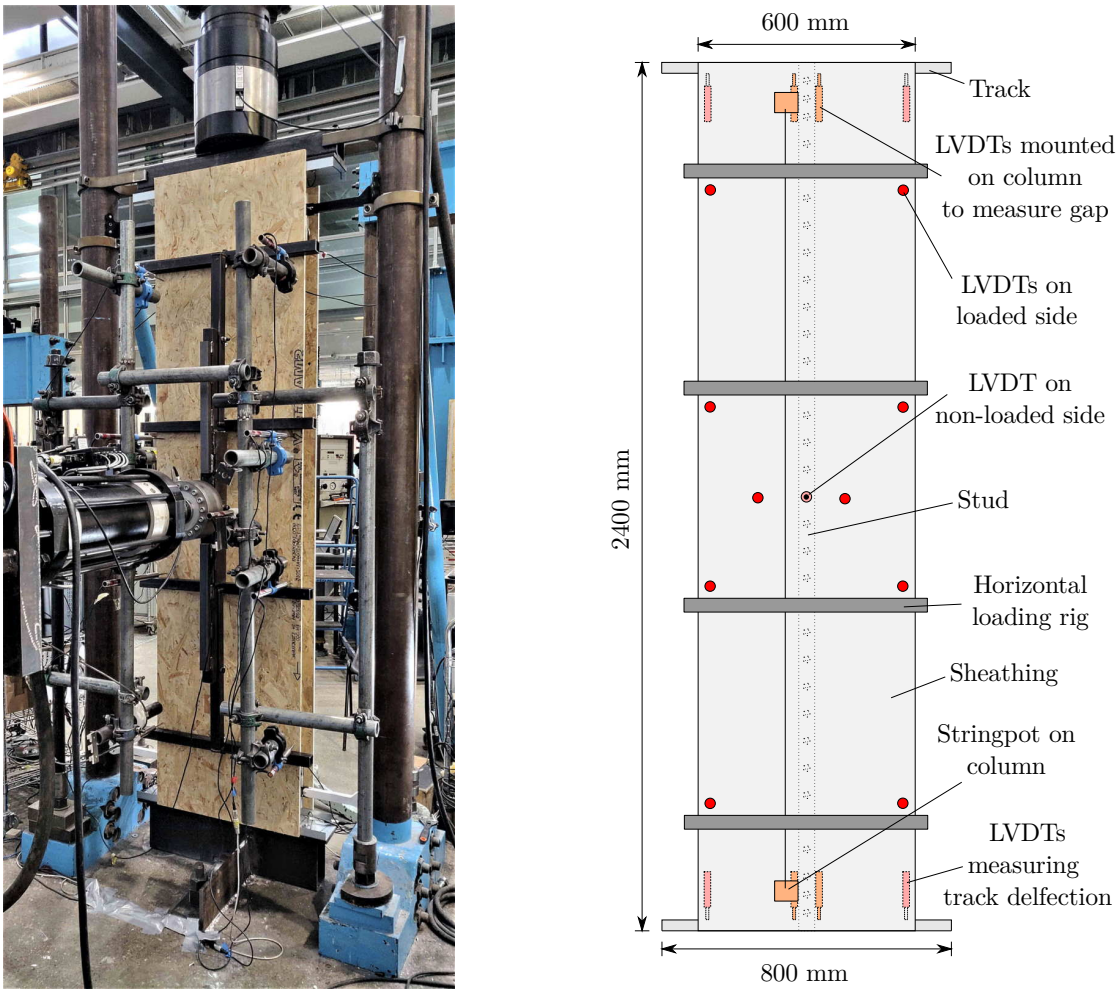

Figure 14: (a) Photo and (b) schematic illustration of test rig with employed instrumentation

In total 19 LVDTs and one string potentiometer were used to measure displacements. Eight LVDTs, along with the string-pot attached to the column, were used to measure the shortening of the column. At each column end, two LVDTs were used to measure the deflection of the track, while two LVDTs mounted on either side of the column measured the closing gap between the column and the track during loading. The net axial shortening of the column was calculated as the difference between the gap closure and track deflection. The axial shortening of the column was also measured using the string potentiometer spanning between the ends of the column, as shown in Figure 14. Ten LVDTs on the laterally loaded

side and one in the centre of the non-loaded side were used to measure lateral displacements. The LVDTs on the loaded side were positioned in the middle of the sheathing and as close as possible to the loading arms of the whiffletree to record the maximum displacement due to bending, as shown in Figure 14. The loads and displacement measurements from the actuators, the LVDTs and the string potentiometer were captured using the DATASCAN [20] acquisition system, recording at a frequency of 1 Hz.

3.6. Boundary and loading conditions

The length of the tracks of the tested specimens was 800 mm, as shown in Figure 14 (b). Detailed views of the top and bottom tracks connected to the test rig are shown in Figure 15, where the 6 mm in diameter anchor bolts with washers are also shown; these were used to secure the tracks to the hot-rolled steel sections. The connection between the column and the track is shown in Figure 16.

The boundary conditions at the member ends derived from the direct contact between the column ends and the web of the tracks. As such, the ability for the column ends to rotate depended on the applied axial load level. For low axial load levels, the boundary conditions were approximately pinned, while for higher axial load levels, increased end fixity arose. The bending moment diagram under the four-point loads and under an equivalent uniformly distributed load assuming pinned end conditions is shown in Figure 17 (a), while, in Figure 17 (b), the corresponding bending moment diagrams assuming fixed boundaries are shown. The total length of the column is designated by L and the horizontal load by H.

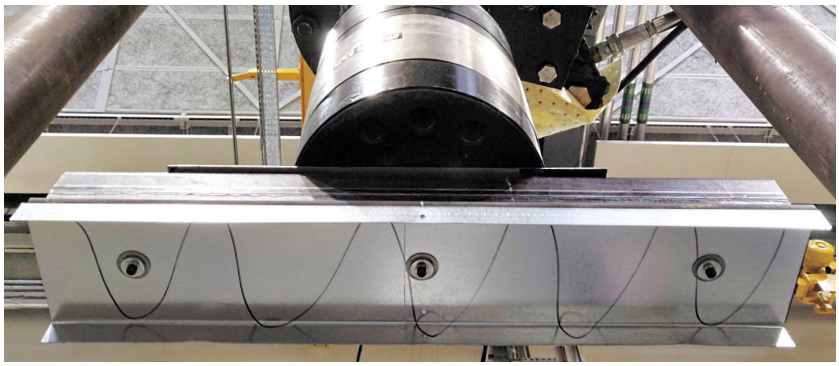

(a)

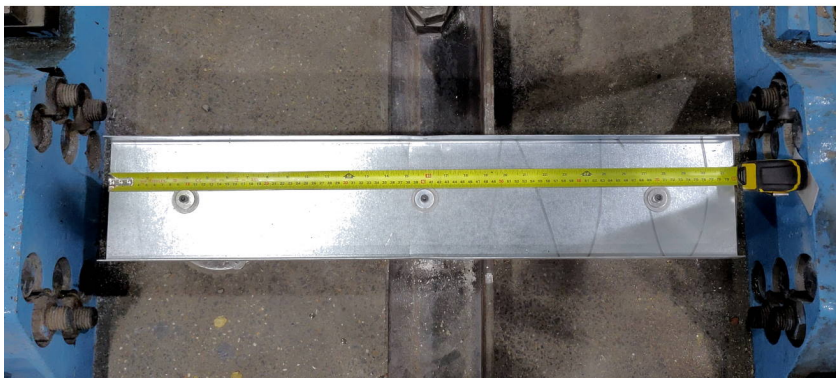

(b)

Figure 15: (a) Top and (b) bottom tracks connected to the test rig

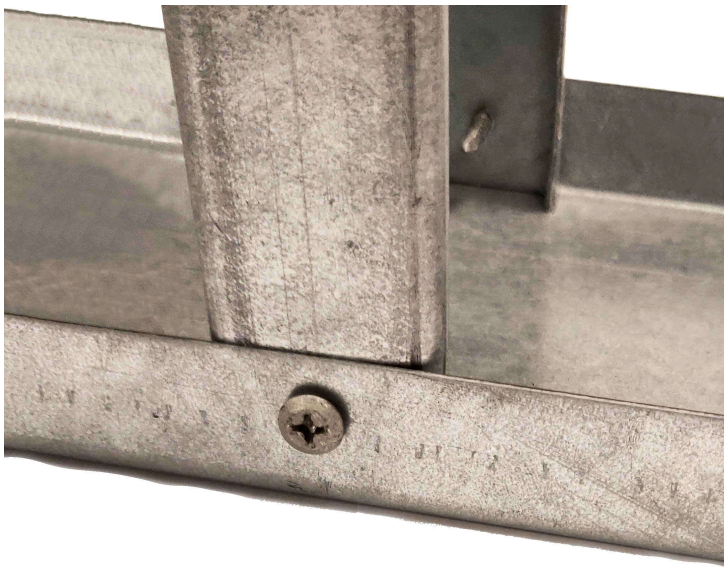

Figure 16: Column-to-track connection

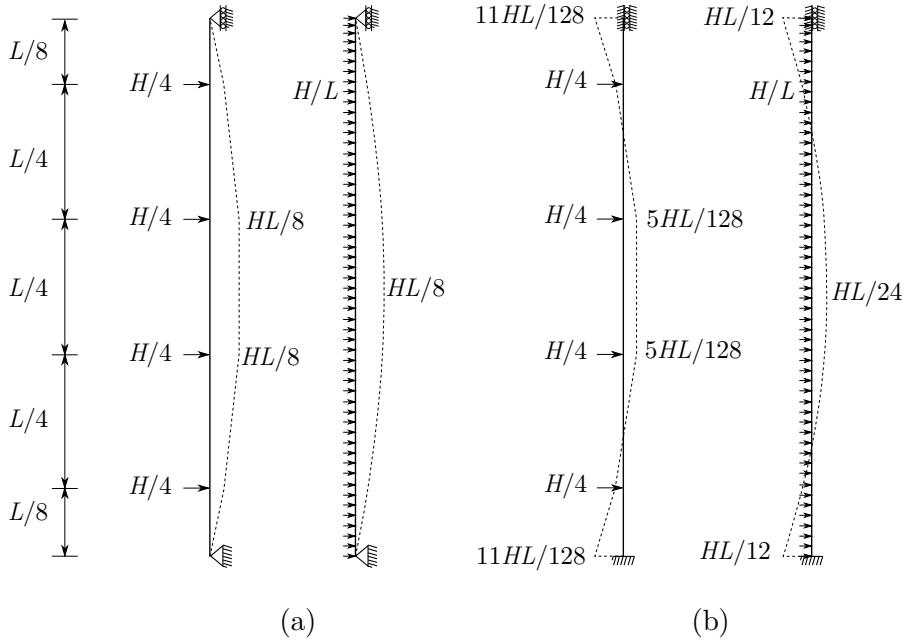

Figure 17: Bending moment diagrams under 4-point loads and the equivalent uniformly distributed load for (a) pinned and (b) fixed boundary conditions

The axial load was applied using displacement control at a rate of 0.25 mm/min while the horizontal load was applied at a rate of 2.00 mm/min also under displacement control. The specimens subjected to pure compression or pure bending were loaded beyond the ultimate load, until a load decrease could be clearly observed. For the combined load cases, the specimens were first axially loaded to a pre-determined load level; the axial load was then held constant under load control, while the horizontal load was increased until failure occurred.

4. Experimental results

A total of 17 member tests were conducted, with eight specimens subjected to pure compression, six to combined compression and bending and three to pure bending. The tested members were sheathed with the same type of board and using the same number of screws on both sides. A summary of the test details and results, including the type of sheathing used, the spacing between the screws, the axial load P_u and horizontal load H_u

at failure and the mode(s) of failure, is provided in Table 6. The notation used for each test in Table 6 begins with the letter G for plasterboard (gypsum) or O for OSB, then with the level of the applied compressive load (expressed as a percentage of the compressive strength of the stud, as determined through the testing performed herein), followed by the letter S and finally by the spacing between the screws in mm. For repeat specimens, 1 or 2 was added at the end of their notation to differentiate between them.

Table 6: Summary of details of the tested specimens and observed failure loads

#	Designation	Sheathing type	Screw spacing	P_u		H_u	Failure mode *
			(mm)	%	(kN)	(kN)	
1	G-100-S600-1	Gypsum	600	100	69.0	0.0	D → CF → FT
2	G-100-S600-2	Gypsum	600	100	77.7	0.0	D → CF → FT
3	G-100-S300-1	Gypsum	300	100	76.5	0.0	(L + D (hole)) → CF
4	G-100-S300-2	Gypsum	300	100	82.1	0.0	(D → CF) + $L_{(end)}$
5	G-100-S150	Gypsum	150	100	85.5	0.0	(L (end) + D) → CF
6	G-100-S75	Gypsum	75	100	90.5	0.0	L (end)
7	O-100-S600	OSB	600	100	79.5	0.0	L (end) + D
8	O-100-S75	OSB	75	100	90.7	0.0	L (end)
9	O-75-S600	OSB	600	75	60.0	14.0	L (hole)
10	O-75-S75	OSB	75	75	67.5	15.5	L (hole)
11	O-50-S600	OSB	600	50	40.0	17.4	L (hole)
12	O-50-S75	OSB	75	50	45.0	21.3	L (end) + L (hole)
13	O-25-S600	OSB	600	25	20.0	20.8	L (hole)
14	O-25-S75	OSB	75	25	22.5	23.5	L (end) + L (hole)
15	O-0-S600	OSB	600	0	0.0	20.8	L + L (end)
16	O-0-S75-1	OSB	75	0	0.0	22.3	L (end) + CF (column-to-track)
17	O-0-S75-2	OSB	75	0	0.0	20.8	L (end) + CF(column-to-track)

* CF: connector failure, L: local buckling, D: distortional buckling, FT: flexural torsional buckling

Six of the specimens under pure compression were sheathed with plasterboard and two with OSB. For the specimens sheathed with plasterboard, all four connector spacings were examined, i.e. 600 mm, 300 mm, 150 mm and 75 mm - as illustrated in Figure 12 while, for

the specimens sheathed with OSB, only the two extreme spacings of 600 mm and 75 mm were studied.

Following testing of the plasterboard specimens under pure compression, and since pull-through failure was prominent, it was decided that the specimens to be tested under combined loading and pure bending would be sheathed with OSB only, with connectors spaced either at every 600 mm or 75 mm. Six tests were conducted under combined load, where the axial compression level was set to 75%, 50% and 25% of the stud compression resistance, which had been determined based on the two tests with OSB sheathing under pure compression.

4.1. Pure compression test results

A summary of the results of the pure compression tests is shown in Figure 18, where the failure load P_u is plotted against the employed spacing of connectors. Substantial increases in capacity can be observed with decreasing connector spacing (from 600 mm to 75 mm), with a 14% increase attained for the OSB sheathed specimens and 23% increase, on average, for the plasterboard sheathed specimens. Note that, in addition to the individual experimental results, an average line between the repeat tests has also been plotted for the plasterboard specimens to highlight the trend in the data. For all the specimens connected at 300 mm and 600 mm intervals, pull-through failure of the connectors, exacerbated by distortional buckling of the flanges (see Figure 19 (a)), was observed; this was followed by sudden flexural torsional buckling of the column once the connection to the sheathing was lost. For the member sheathed with plasterboard and connected at 150 mm intervals, screw pull-through failure initiated at the top end of the specimen; this then led to the further development of local and distortional buckling and eventually to overall member failure. For the specimens with a connector spacing of 75 mm, pull-through of the screws was prevented and failure was triggered by local buckling near the bottom end of the columns. For the specimens sheathed with OSB, failure was due to a combination of distortional and local buckling; the specimen connected at 75 mm intervals reached a higher capacity due to the greater restraint provided by the screw connectors.

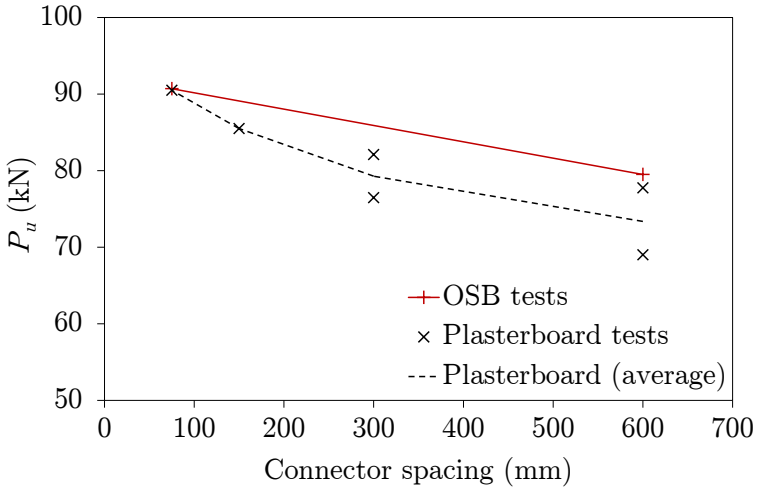

Figure 18: Ultimate load plotted against connector spacing for specimens under pure compression

(a) (b)

Figure 19: Typical failure modes: (a) distortional buckling (and pull-through failure of connectors) for a member under compression and (b) local buckling at a service hole for a member under bending

4.1.1. Boundary conditions under pure compression

The boundary conditions at the ends of the specimens under pure compression, set in tracks and connected at the flanges through screws, are effectively clamped due to the

presence of the applied axial force – upon rotation of the end cross-section about either edge, a restoring moment $M_R = Ph/2$ is generated about that edge by the centroidally-acting axial force, leading to fixed boundary conditions – see Figure 20. This is particularly clear, and supported by the observed experimental results in this study and reported findings in the literature [7, 21], for deeper members (larger h), but may diminish for shallower (smaller h) members.

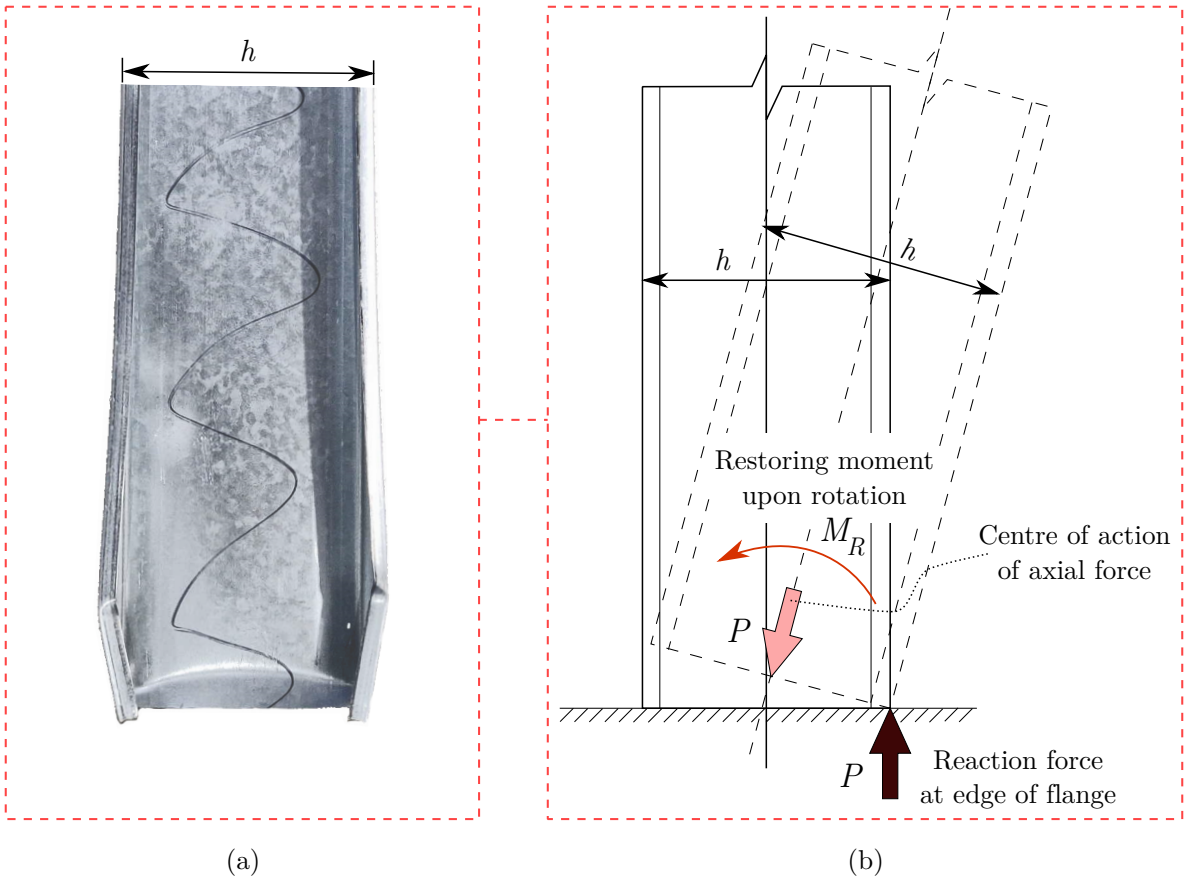

Figure 20: (a) Typical end failure mode for specimens under pure compression and (b) schematic illustration of end fixity arising due to the restoring moment from axial force. Note that the overall end rotation illustrated in (b) is prevented in the real system, as seen in (a), due to the action of the restoring moment.

4.1.2. Load-displacement curves under pure compression

Load-displacement curves derived from different measurement devices – the vertical actuator, the string potentiometer attached to the column and the difference between the

measurements of the LVDTs positioned on the tracks and on the column measuring the gap between them – of a typical specimen under compression (G-100-S75) are shown in Figure 21. As shown in the figure, the load-displacement response based on the displacements recorded by the actuator exhibited a substantially lower stiffness than the theoretical axial stiffness of the column EA/L (where E is the Young's modulus of the steel, A is the cross sectional area of the column and L is the length of the column), with the gradual increase of stiffness at the beginning of the curve corresponding to the gradual closure of the gap between the track and the column. Since the string potentiometer was not measuring across the gap, the resulting initial stiffness of the member closely matches the theoretical axial stiffness. Deviations at higher loads relate to the asymmetric nature of the measurements, which were taken on one side of the specimens only. Finally, the curve calculated based on the difference of the LVDT readings measuring the deflection of the tracks and the gap closure between the track and column (see Figure 14 (b)) closely matches the general response of the column.

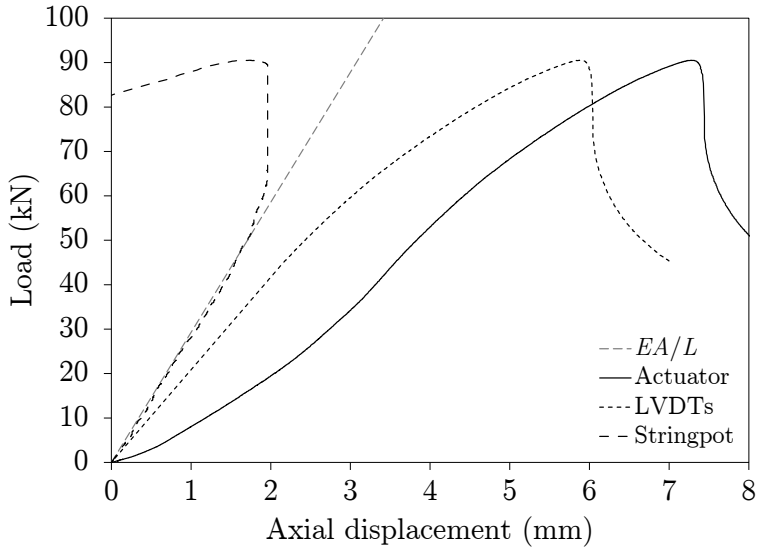

Figure 21: Axial load-displacement curves of a typical specimen under pure compression

For all specimens under pure compression, the reported load-displacement curves are based on the LVDT measurements, after correction of the full curves, using Equation (6), based on the 'true' initial stiffness captured from the stringpot, which closely matches the

axial stiffness EA/L, as described below.

$$\delta_{true} = \delta_{LVDT} - \left(\frac{P}{k_{LVDT}} - \frac{P}{k_{stringpot}} \right) \tag{6}$$

In Equation (6), δ_{true} is the adjusted axial displacement, δ_{LVDT} is the axial displacement based on the LVDT measurements, P is the axial load, $k_{stringpot}$ is the initial stiffness from the stringpot curve and k_{LVDT} is the initial stiffness from the LVDT curve; the initial stiffnesses were determined based on measurements up to about 40% of the peak load where the response remained approximately linear. Adjustment of a full axial load-displacement curve using Equation (6) for a typical specimen (G-100-S75) is demonstrated in Figure 22.

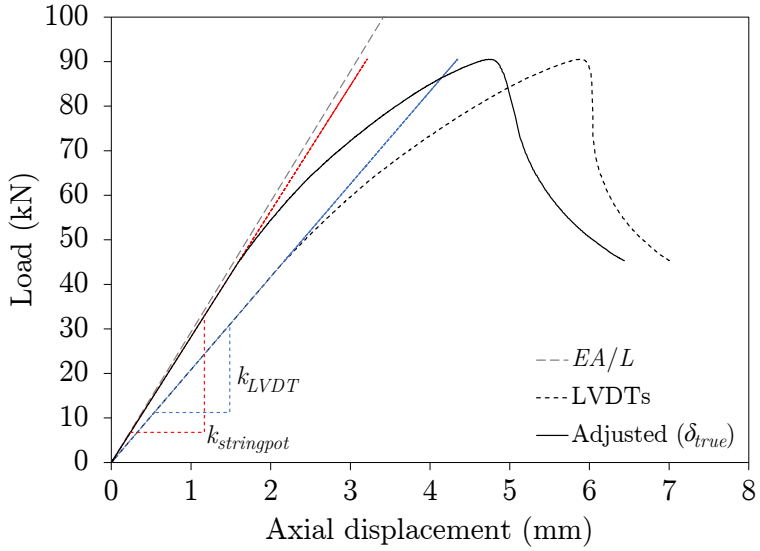

Figure 22: Adjustment of gradient for the results of axial load-displacement curves

The axial load-displacement curves for the OSB sheathed specimens are presented in Figure 23, while the corresponding curves for the specimens sheathed with plasterboard are shown in Figure 24. The discontinuities that can be seen in the specimens sheathed with plasterboard (Figure 24) and connected at 150 mm, 300 mm and 600 mm intervals correspond to failure of individual connectors.

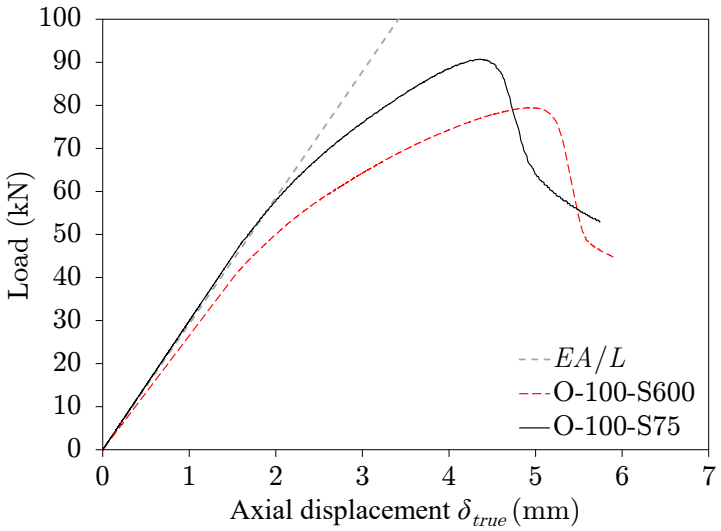

Figure 23: Axial load-displacement curves of specimens sheathed with OSB under compression

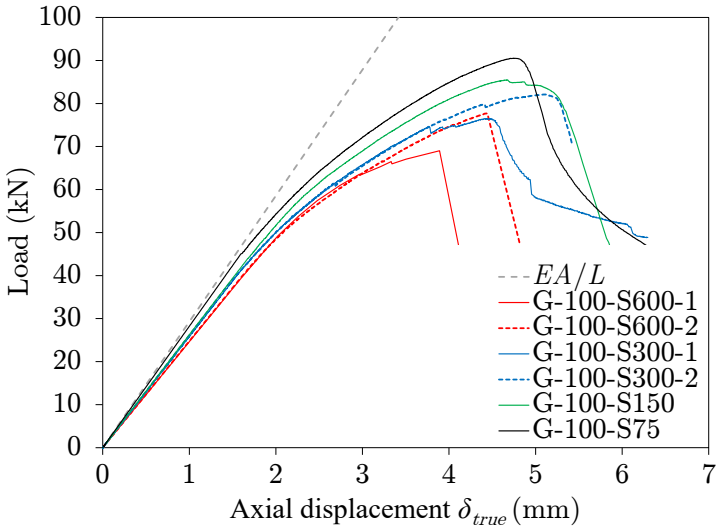

Figure 24: Axial load-displacement curves of specimens sheathed with plasterboard under compression

A comparison between the specimens sheathed with OSB and plasterboard and subjected to pure compression is presented in Figure 25. As expected, it can be observed that the stiffness and capacity of the specimens increases with increasing numbers of connectors due to the additional restraint to both the global and cross-sectional buckling modes. The specimens with the connectors spaced at 75 mm intervals exhibited similar peak capacities, although a slightly higher stiffness was observed for the specimens sheathed with OSB.

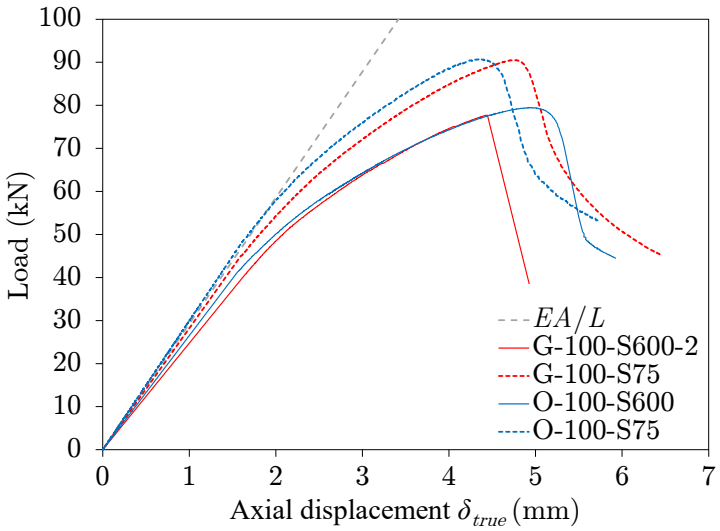

Figure 25: Comparison between the axial load-displacement curves of specimens sheathed with plasterboard and OSB under compression

The failure modes of the columns sheathed with plasterboard are shown in Figure 26. For the specimens that were connected at 600 mm and 300 mm intervals, distortional buckling developed between the connectors, while the specimens connected every 150 mm and 75 mm suffered local buckling failure near the column ends.

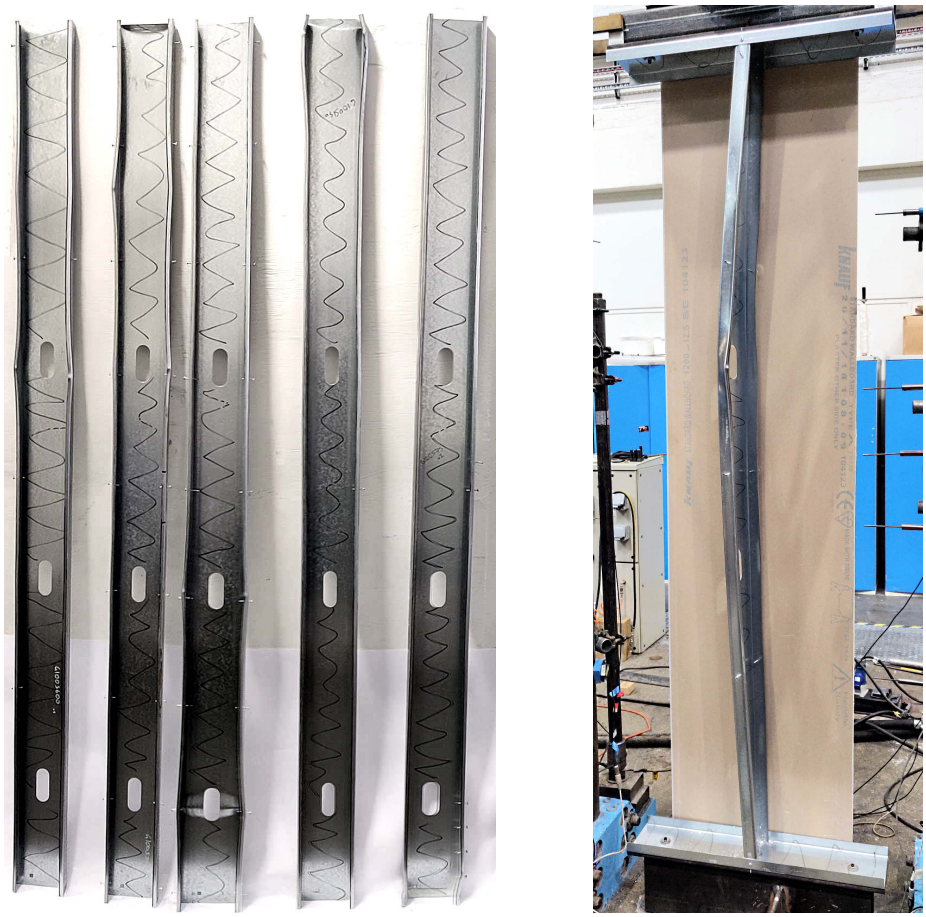

(a) (b)

Figure 26: (a) Failure modes of columns sheathed with plasterboard and tested under compression (from left to right – connectors spaced at 600 mm, 300 mm (2 repeated), 150 mm and 75 mm), (b) test specimen with 600 mm connector spacings, post failure (with the sheathing removed to observe the failure mode)

4.2. Compression and bending test results

The results from the combined compression and bending tests are presented in Figure 27, where the ultimate compression loads P_u are plotted against the ultimate horizontal loads H_u; a distinction is made between the OSB-sheathed specimens with connectors spaced at 600 mm and 75 mm intervals. Increased capacities in both compression and bending (between 15 – 20%) were attained when closer-spaced connectors were employed. It should be mentioned that the capacity of the specimens tested under pure bending was limited by the strength of the connection between the track and the column.

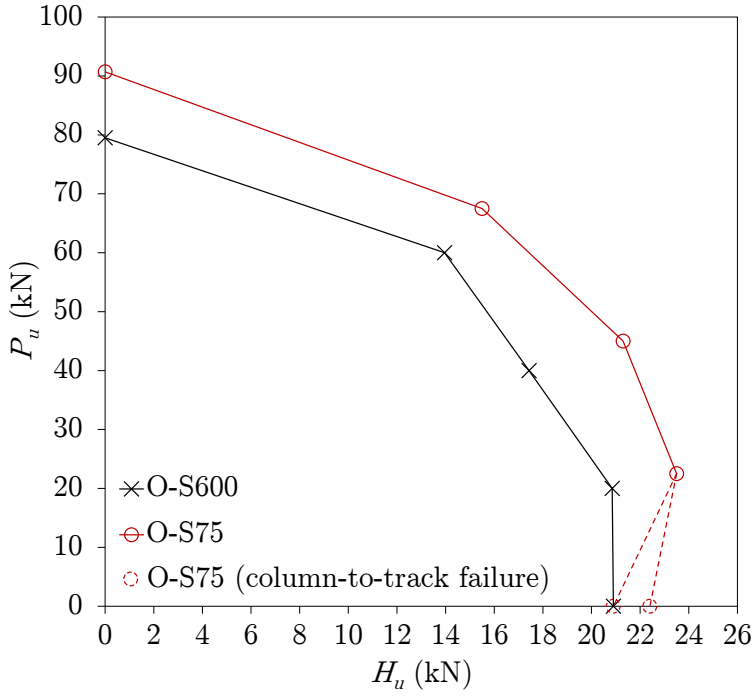

Figure 27: Ultimate compression (P_u) and horizontal (H_u) loads for beam-column specimens sheathed with OSB and connected at 600 mm and 75 mm intervals

290 The dominant failure mode of the OSB-sheathed beam-column specimens was local failure at the service openings and at the ends of the members, as shown in Figure 28. For the specimens under pure bending with the connectors spaced at 75 mm, shear failure of the screws between the main member and track occurred – see Figure 28 (b), without which, higher load-bearing capacities were anticipated.

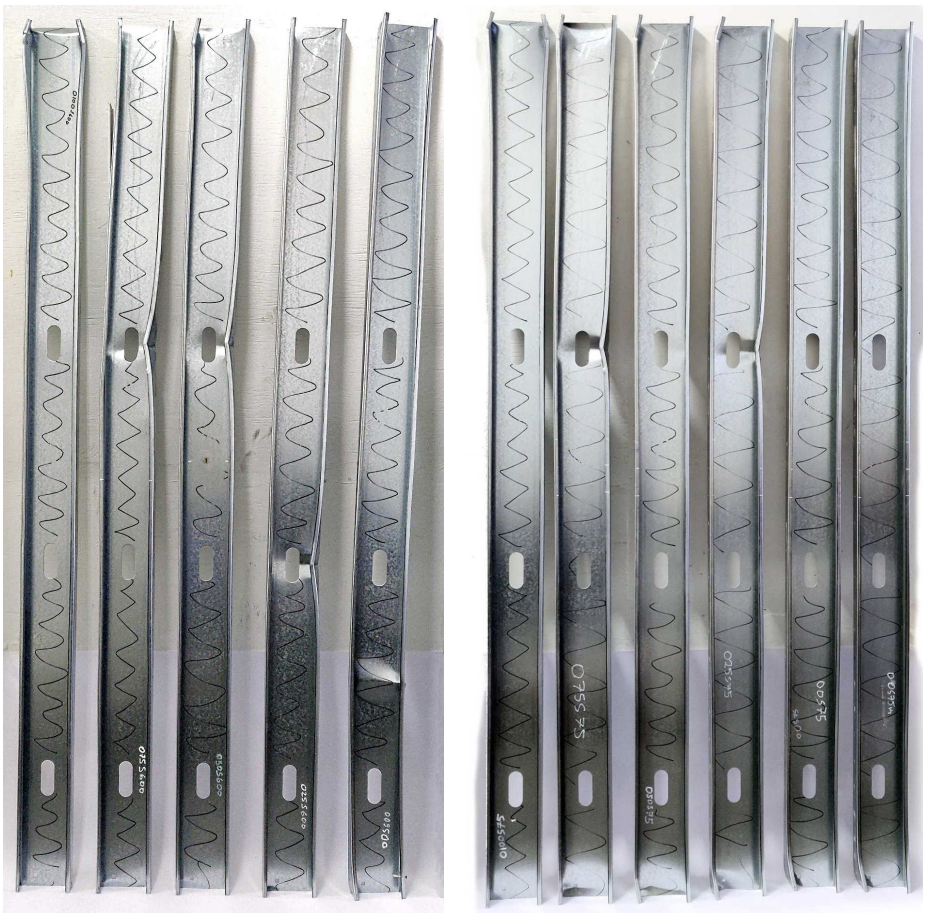

(a) (b)

Figure 28: Failure modes of all the tests specimens (from left to right – 100% compression to 100% bending) with OSB sheathing connected at (a) 600 mm spacings and (b) 75 mm spacings

4.2.1. Load-displacement curves

The horizontal load versus mid-height displacement curves for the OSB sheathed beam-columns are shown in Figures 29 and 30 for the specimens connected at 75 mm and 600 mm spacings respectively; all tested specimens are plotted together in Figure 31. Note that the horizontal mid-height displacement was calculated by averaging the three LVDT measurements at mid-height (from the two LVDTs on the loaded side and the third on the non-loaded side – see Figure 14 (b)). The full load-deflection curves are shown in Figure 31 (a) while their initial part is presented in Figure 31 (b), where lines corresponding to the theoretical linear response in the case of pinned and fixed boundary conditions are also

plotted. The theoretical responses were calculated assuming linear, elastic behaviour for the 4-point load configuration illustrated in Figure 17; the calculated mid-height deflections (δ_p and δ_f) and stiffnesses (k_p for pinned and k_f for fixed) were determined using Equations (7) and (8), where H is the total horizontal load, L is the length of the member and EI is the sum of the flexural rigidities of the steel member and the two sheathing boards. The calculated k_p and k_f values were 1.29 kN/mm and 6.60 kN/mm respectively.

$$\delta_p = \frac{41HL^3}{3072EI} \quad ; \quad k_p = H/\delta_p = \frac{3072EI}{41L^3} \tag{7}$$

$$\delta_f = \frac{HL^3}{384EI} \quad ; \quad k_f = H/\delta_f = \frac{384EI}{L^3} \tag{8}$$

It was found that the flexural stiffnesses of the specimens with the connectors spaced at 75 mm intervals that were subjected to axial loads corresponding to 75% and 50% of their compressive resistance were approximately 30% and 20% respectively higher than the theoretical flexural stiffness corresponding to a member with pinned-end conditions. For the specimens with connectors spaced at 600 mm intervals under axial loads equal to 75% and 50% of their compressive resistance, the flexural stiffnesses were about 20% and 10% respectively higher than the theoretical value for a pin-ended member. The relative degree of fixity can be expressed as $\beta = (k - k_p)/(k_f - k_p)$, where k is the initial stiffness determined from the horizontal load–mid-displacement curves (where $\beta = 0$ and $\beta = 1$ correspond to pinned and fixed end conditions and all intermediate values i.e. $0 \leq \beta \leq 1$ correspond to the partially restrained end conditions achieved in the tests.

In Figure 32, the relative degree of fixity β is plotted against the percentage of compression for all beam-column specimens. It can be observed that the relative degree of fixity increases with increasing compression and with decreasing connector spacing. This can be explained with reference to Section 4.1.1 and Figure 20, where, as described for the case of pure compression, the applied axial load generates a restoring moment as the member rotates about the outer edge of the cross-section. This effect weakens (or remains active up to lower lateral load levels) as the level of applied compression reduces and as the overturning moment (i.e. the applied bending moment) becomes more dominant [21].

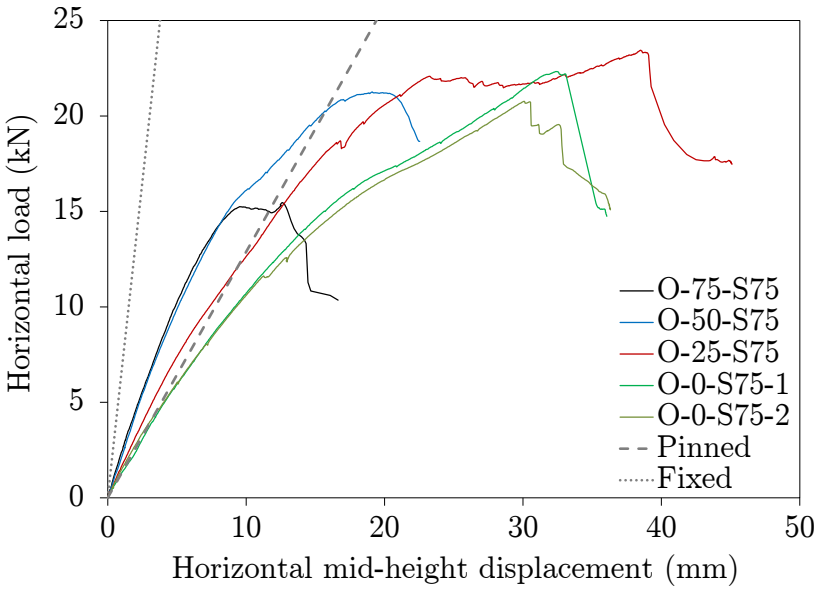

Figure 29: Horizontal load versus mid-height displacement curves for beam-column specimens connected at 75 mm intervals

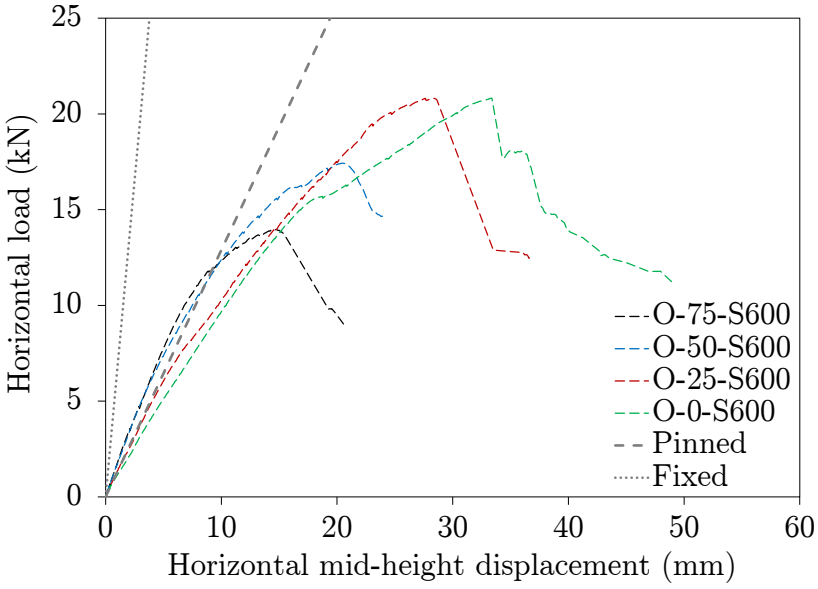

Figure 30: Horizontal load versus mid-height displacement curves for beam-column specimens connected at 600 mm intervals

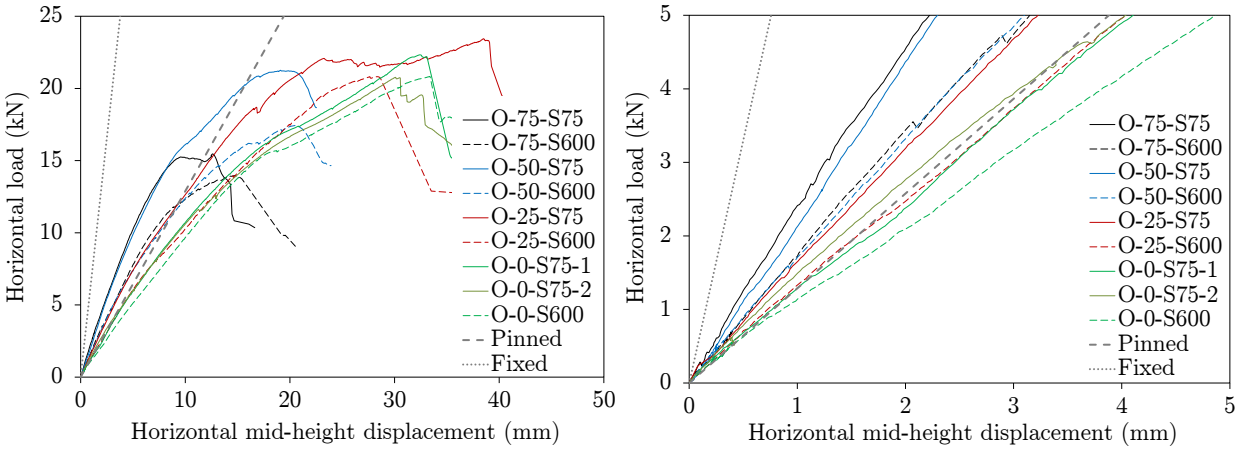

Figure 31: Horizontal load versus mid-height displacement curves for all specimens over (a) full range and (b) initial stages of loading for comparison with the theoretical stiffness for fixed and pinned boundary conditions

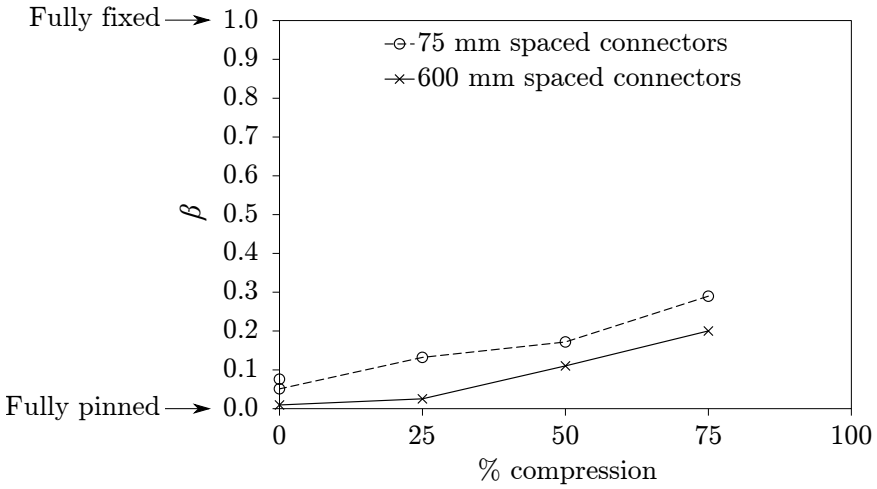

Figure 32: Relative degree of fixity β with increase in compression level for beam-columns based on slope of horizontal load-mid-span deflection curves

4.2.2. Load-rotation curves

Two inclinometers, mounted on the webs of the beam-column specimens at a distance of $L/10$ from each end, were used for determining the near-end rotations of the members during loading. The load-rotation curves, based on the average readings from the two inclinometers (which were close to symmetrical), are presented for the specimens with connector spacings

of 75 mm and 600 mm in Figures 33 and 34 respectively. The theoretical rotations, θ_p and θ_f, at $L/10$ and the rotational stiffnesses, $k_{\theta,p} = H/\theta_p$ and $k_{\theta,f} = H/\theta_f$, corresponding to the member response with pinned and fixed end conditions, calculated according to Equations (9) and (10) respectively, are also plotted. The calculated $k_{\theta,p}$ and $k_{\theta,f}$ values were 17.80 kN/deg and 118.20 kN/deg respectively.

$$\theta_p = \frac{259HL^2}{6400EI}\frac{180}{\pi} \quad ; \quad k_{\theta,p} = H/\theta_p = \frac{320\pi EI}{2331L^2} \tag{9}$$

$$\theta_f = \frac{39HL^2}{6400EI}\frac{180}{\pi} \quad ; \quad k_{\theta,f} = H/\theta_f = \frac{320\pi EI}{351L^2} \tag{10}$$

Similarly to the load-displacement results, the load-rotation results indicate increasing end fixity (or retention of fixity to higher lateral load values) with increasing compression levels and reducing connector spacing. This is shown in Figure 35, where the relative degree of fixity is now expressed in terms of the rotations i.e. $\beta_\theta = (k_\theta - k_{\theta,p})/(k_{\theta,f} - k_{\theta,p})$. The relative degrees of fixity derived from the load-rotation and the load-mid-span displacement curves are very similar (within 5%).

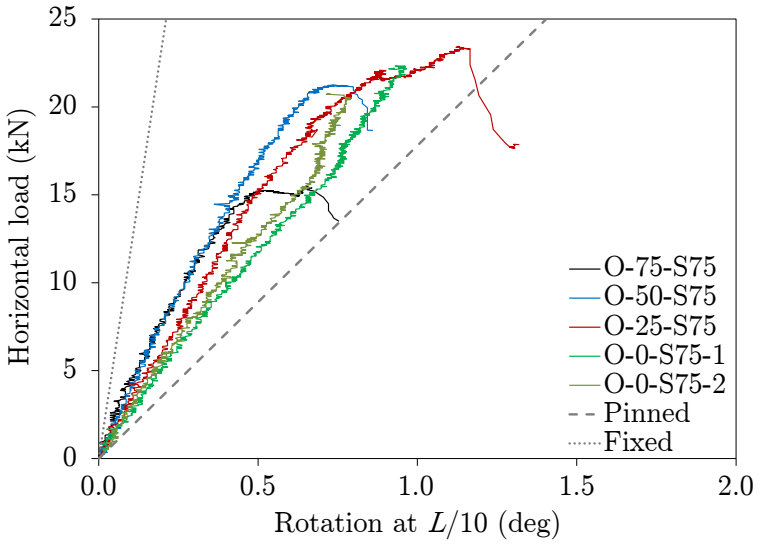

Figure 33: Horizontal load versus rotation at $L/10$ curves for beam-column specimens connected at 75 mm spacings

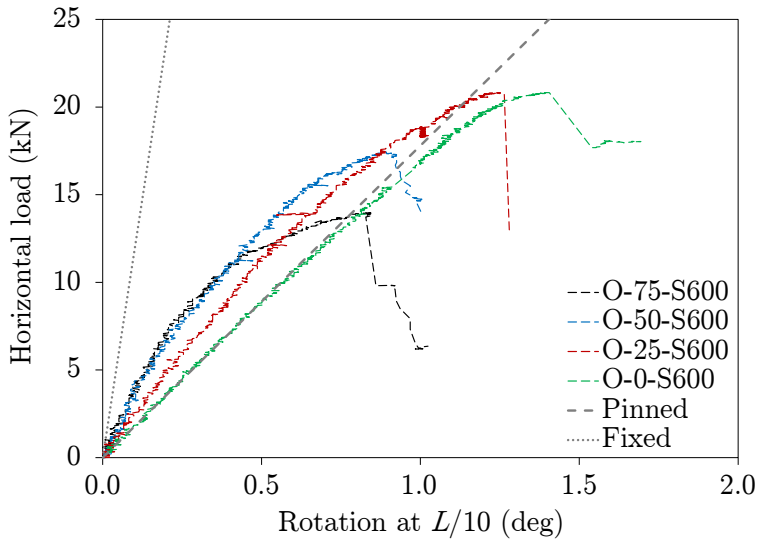

Figure 34: Horizontal load versus rotation at $L/10$ curves for beam-column specimens connected at 600 mm spacings

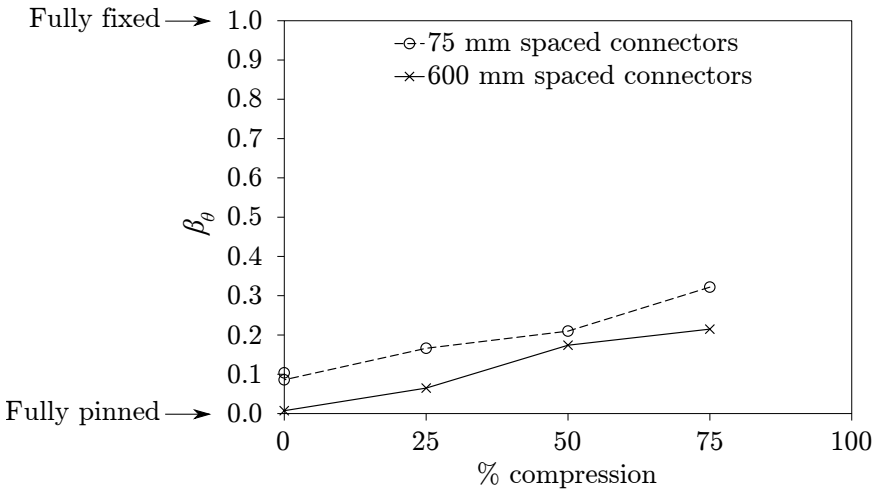

Figure 35: Relative degree of fixity β_θ with increase in compression level for beam-columns based on the slope of horizontal load versus rotation at $L/10$

4.2.3. Strain distributions

For the combined compression-bending specimens and the bending specimens, strain gauges were mounted at the mid-height of the members in the middle of the flanges, as shown in Figure 36 (b). The strain gauges were used to monitor the progression of strain at key locations on the specimens during testing and to verify that the loading was applied as

intended. The two strain gauges mounted on the members are designated as SGT for the one on the tension (or lower compression) flange and SGC for the one on the compression flange. A graph showing the development of strain for the typical case of the O-75-S600 specimen during the compression P and then horizontal H loading stages is illustrated in Figure 36 (a). Three key points are highlighted in Figure 36: ① at the pre-determined compression load P_u (75% of the pure compressive resistance for the case illustrated) prior to the application of any horizontal load, ② at P_u and 50% of ultimate horizontal load H_u and ③ at P_u and 100% of H_u. The similarity of compressive strains in the compression stage and symmetry (i.e. approximately equal and opposite strains) in the bending stage confirm that the test setup and specimens performed as intended.

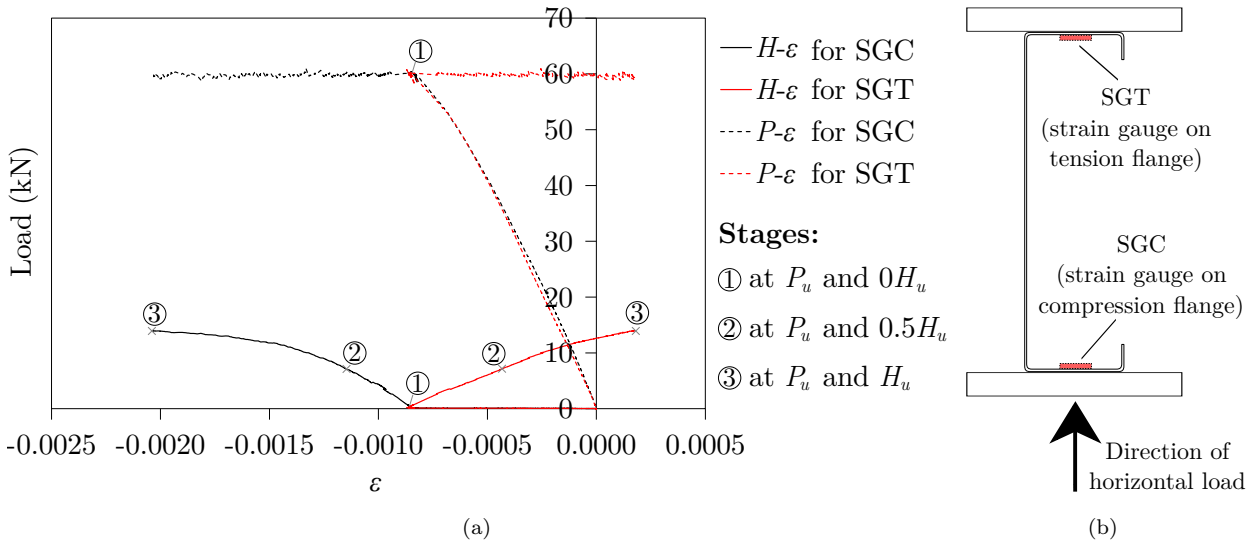

Figure 36: Strain gauge results from beam-column tests showing (a) development of strain for specimen O-75-S600 and (b) position of strain gauges at mid-height of member

5. Comparison of experimental results with existing findings and code provisions

5.1. Comparison with previous experimental findings in the literature

The findings of Vieira et al. in [7], in which the screw connectors in sheathed cold-formed steel members were shown to provide effective restraint against global buckling modes, have been supported by the research presented herein. Full restraint to the global modes, such

that local/distortional buckling only became the controlling failure modes, was achieved in the present study for specimens with the more substantial interconnection, as also found in [7]. With regards, to the end fixity achieved in cold-formed steel wall systems, as also indicated by Peterman et al. [2, 11] under pure bending, the end conditions are close to pinned, but as the level of axial load and the degree of interconnectivity increases, there is a transition towards fixed ended boundary conditions.

5.2. Comparison with Eurocode 3 design provisions

The compression capacities of the sheathed specimens, even for the widest connector spacing, were found to be significantly higher than those predicted using EN 1993-1-1 [22] and EN 1993-1-3 [19] with typical design assumptions, including that of pinned boundary conditions at the member ends. Comparisons between the Eurocode 3 axial resistance predictions and the obtained test results are provided in Figure 37. Note that the calculation of the cross-sectional compression resistance $N_{c,Rd}$, loss of effectiveness due to local and distortional buckling was accounted for in line with the EN 1993-1-3 [19] provisions. The member resistances (i.e. the flexural buckling resistances about the major $N_{b,y,Rd}$ and minor $N_{b,z,Rd}$ axis, the torsional buckling resistance $N_{b,T,Rd}$ and the flexural-torsional buckling resistance $N_{b,FT,Rd}$) were initially calculated with the effective lengths for buckling about the major $L_{eff,y}$ and minor $L_{eff,z}$ axes taken as the full member length (2.4 m). This typical design assumption [23] presupposes that no restraint is provided by the sheathing; the results are shown in Figure 37 (a). Equivalent comparisons are presented in Figure 37 (b), but with the effective length for buckling about the minor axis $L_{eff,z}$ taken equal to the spacing of the connectors. As shown in Figure 37 (a), without any restraint assumed from the sheathing, the test results are underestimated by about three to four times, with $N_{b,z,Rd}$ being the critical resistance. On the other hand, as shown in Figure 37 (b), taking $L_{eff,z}$ equal to the connector spacing leads to unsafe predictions for the plasterboard sheathed specimens connected at 300 mm and 600 mm intervals which suffered connector failure, but safe-sided predictions for the OSB-sheathed specimens where connector failure did not occur. An intermediate condition with $L_{eff,z}$ taken as twice the connector spacing, effectively assuming

that every other connector has failed and does not contribute any restraint, is presented in Figure 37 (c) yielding safe-sided predictions for the specimens suffering connector failure.

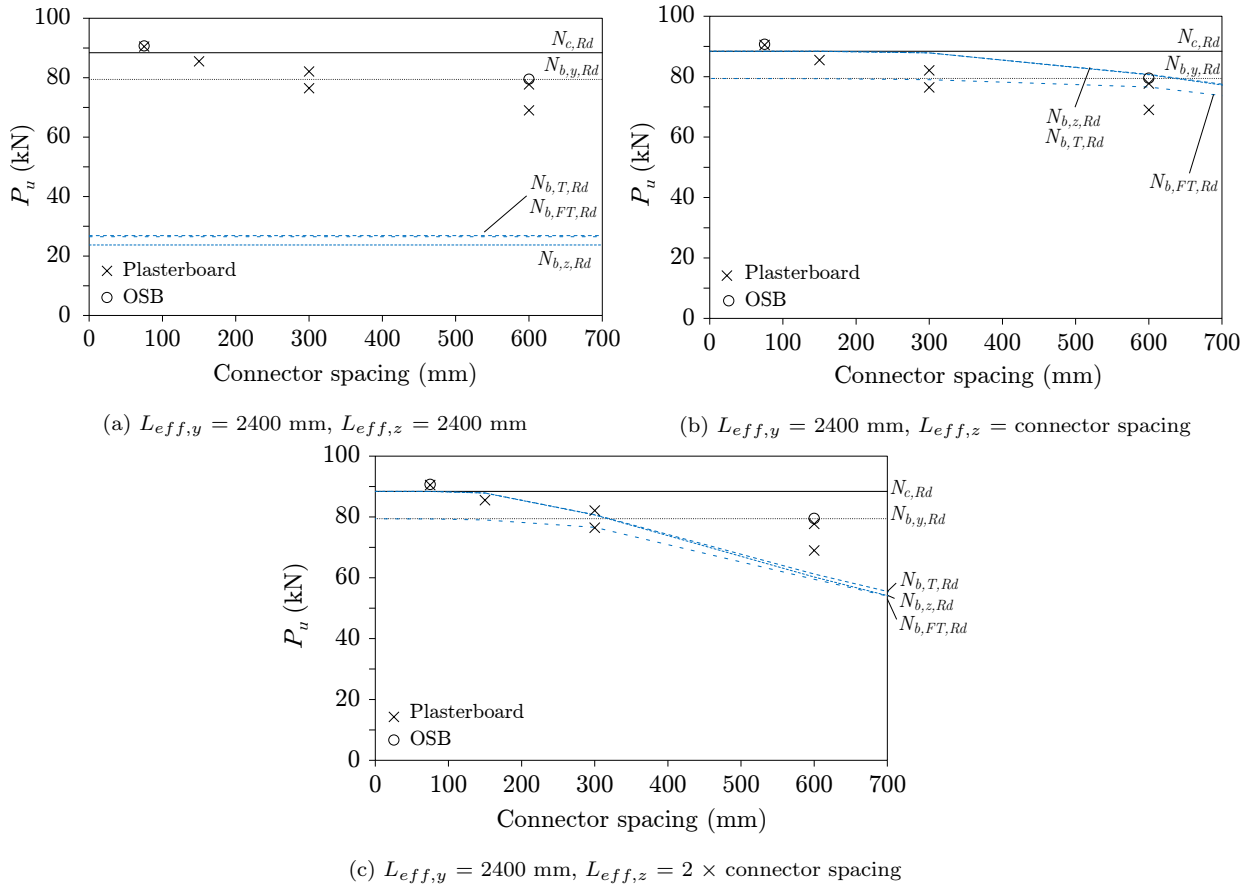

(a) $L_{eff,y}$ = 2400 mm, $L_{eff,z}$ = 2400 mm

(b) $L_{eff,y}$ = 2400 mm, $L_{eff,z}$ = connector spacing

(c) $L_{eff,y}$ = 2400 mm, $L_{eff,z}$ = 2 × connector spacing

Figure 37: Comparisons between compression test results and Eurocode 3 resistance predictions with different assumptions made for $L_{eff,z}$ equal to (a) the full column length of 2400 mm (b) the connector spacing and (c) two times the connector spacing. $L_{eff,y}$ was taken as the full member length in all cases.

The beam-column test results are compared with the EN 1993-1-3 [19] interaction curve, given by Equation (11), in Figure 38. The design assumptions that have been considered are: (i) no restraint from the sheathing (ii) $L_{eff,z}$ = 600 mm and (iii) $L_{eff,z}$ = 75 mm. Note that the effective length about the major axis $L_{eff,y}$ was taken as the full length of the member in all cases.

$$\left(\frac{P_u}{N_{b,Rd}}\right)^{0.8} + \left(\frac{M_u}{M_{b,Rd}}\right)^{0.8} \leq 1.0 \tag{11}$$

In Equation (11) $N_{b,Rd}$ is taken as the minimum of $N_{c,Rd}$, $N_{b,y,Rd}$, $N_{b,z,Rd}$, $N_{b,T,Rd}$ and

$N_{b,FT,Rd}$, while $M_{b,Rd}$ is the lateral torsional buckling resistance. Note, that calculation of the effective section properties for both compression and bending (i.e. the effective area and section modulus) was carried out by including iteration of the effective thickness for the effects of distortional buckling, while the influence of rounded corners was taken into account by using the mid-line design provisions in [19].

As shown in Figure 38, assuming that the members have pinned end conditions and that no restraint is offered by the sheathing (i.e. $L_{eff,y} = L_{eff,z}$ = full member length) yields very conservative resistance predictions, while recognising the restraint from the connectors leads to considerably more accurate predictions, provided the connectors possess sufficient capacity [2, 18, 24]. The accuracy of the resistance predictions is however limited by the shape of the interaction curve set out in EN 1993-1-3 [19]. In particular, the concave nature of the curve, arising from the value of the powers in Equation (11) being 0.8 does not match the convex trend of the test data points. This, together with the features described above and also potential for composite action [25], are being explored in a parallel numerical study to support the development of design rules that explicitly recognise the contribution of the sheathing and interconnection with the studs in cold-formed steel wall systems.

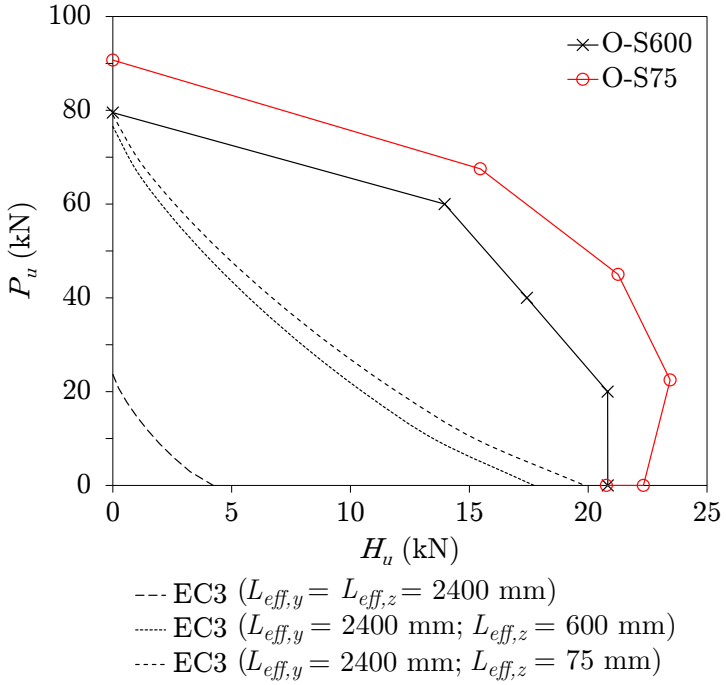

Figure 38: Comparison between tests results and Eurocode 3 resistance predictions assuming various effective lengths

6. Conclusions

An experimental study into the structural performance of sheathed cold-formed steel members has been presented in this paper. Seventeen full-scale tests, comprising eight specimens under pure compression, six specimens under combined loading and three under pure bending, were carried out, along with supporting material tests and imperfection measurements. The tested specimens were sheathed with either plasterboard or OSB, on both sides, with various stud-to-sheathing connector spacings ranging from 600 mm to 75 mm.

When subjected to pure compression, the controlling failure mode exhibited by the studs connected to plasterboards at the wider spacings (i.e. 600 mm and 300 mm) was pull-through of the connectors, while for the studs sheathed with OSB and plasterboard at the denser connector spacings of 150 mm and 75 mm, local buckling was the dominant failure mode. For the OSB-sheathed beam-column specimens local failure at the service openings was observed, while for the specimens subjected to pure bending, local buckling and stud-to-

track connector failure occurred.

Reducing the spacing of the connectors from 600 mm to 75 mm resulted in up to 20% increases in the capacity of the specimens sheathed with OSB under both compression and bending. For the specimens sheathed with plasterboards and subjected to pure compression, reducing the connector spacing from 600 mm to 75 mm resulted in up to 30% increases in capacity while pull-through connector failure was also prevented. It should of course be noted that additional fixings come at a cost and that there is a tradeoff between structural performance and practicality of installation

Initial comparisons with existing design guidance revealed that if the effect of the sheathing is not considered, very conservative resistance predictions are obtained. Development of design rules that recognise the restraint, end fixity and potential composite action present in sheathed cold-formed steel wall systems, supported by a parallel numerical study, is currently underway.

Data availability

The data presented herein are available from the corresponding author, upon reasonable request.

Acknowledgements

For his assistance and guidance in the structural laboratory special thanks are given to Les Clark. Funding for this research was received from the EPSRC Centre for Doctoral Training in Sustainable Civil Engineering at Imperial College London and Ayrshire Metals Limited.

References

[1] J. L. C. M. Vieira, B. W. Schafer, Behavior and design of sheathed cold-formed steel stud walls under compression, Journal of Structural Engineering 139 (5) (2013) 772–786.

[2] K. D. Peterman, B. W. Schafer, Sheathed cold-formed steel studs under axial and lateral load, Journal of Structural Engineering 140 (10) (2014) 04014074.

[3] A. Simaan, T. Peköz, Diaphragm braced members and design of wall studs, Journal of the Structural Division, ASCE 102 (1) (1976) 77–92.

[4] T. H. Miller, T. Peköz, Behavior of gypsum-sheathed cold-formed steel wall studs, Journal of Structural Engineering 120 (5) (1994) 1644–1650.

[5] Y. S. Tian, J. Wang, T. J. Lu, C. Y. Barlow, An experimental study on the axial behaviour of cold-formed steel wall studs and panels, Thin-Walled Structures 42 (4) (2004) 557–573.

[6] Y. Telue, M. Mahendran, Behaviour and design of cold-formed steel wall frames lined with plasterboard on both sides, Engineering Structures 26 (5) (2004) 567–579.

[7] J. L. C. M. Vieira, Y. Shifferaw, B. W. Schafer, Experiments on sheathed cold-formed steel studs in compression, Journal of Constructional Steel Research 67 (10) (2011) 1554–1566.

[8] D. C. Fratamico, S. Torabian, X. Zhao, K. J. R. Rasmussen, B. W. Schafer, Experimental study on the composite action in sheathed and bare built-up cold-formed steel columns, Thin-Walled Structures 127 (2018) 290–305.

[9] R. M. Lawson, A. G. Way, M. Heywood, J. B. P. Lim, R. Johnston, K. Roy, Stability of light steel walls in compression with plasterboards on one or both sides, Proceedings of the Institution of Civil Engineers-Structures and Buildings (2019) 1–19.

[10] S. Selvaraj, M. Madhavan, Studies on cold-formed steel stud panels with gypsum sheathing subjected to out-of-plane bending, Journal of Structural Engineering 144 (9) (2018) 04018136.

[11] K. D. Peterman, Experiments on the stability of sheathed cold-formed steel studs under axial load and bending, MSc thesis, Johns Hopkins University, Baltimore, Maryland, USA (2012).

[12] BS EN 10346, Continuously hot-dip coated steel flat products for cold forming — Technical delivery conditions, BSI (2015).

[13] BS EN 10143, Continuously hot-dip coated steel sheet and strip — Tolerances on dimensions and shape, BSI (2006).

[14] EN ISO 6892, Metallic materials - Tensile testing. Part 1: Method of test at room temperature, European Committee for Standardization, Brussels, Belgium (2016).

[15] EN 520, Gypsum plasterboards — Definitions, requirements and test methods, European Committee for Standardization, Brussels, Belgium (2009).

[16] EN 300, Oriented Strand Boards (OSB) — Definitions, classification and specifications, European Committee for Standardization, Brussels, Belgium (2006).

[17] EN 789, Timber structures. Test methods. Determination of mechanical properties of wood based panels, European Committee for Standardization, Brussels, Belgium (2005).

[18] C. Kyprianou, P. Kyvelou, L. Gardner, D. A. Nethercot, Characterisation of material and connection behaviour in sheathed cold-formed steel wall systems - Part 1: Experimentation and data compilation,

Structures 30 (2021) 1161–1183.

[19] EN 1993-1-3, Eurocode 3: Design of steel structures — Part 1-3: General rules — Supplementary rules for cold-formed members and sheeting, European Committee for Standardization, Brussels, Belgium (2006).

[20] Datascan, Datascan acquisition system, Carollton, Texas, USA (2019).

[21] X. Yun, L. Gardner, The continuous strength method for the design of cold-formed steel non-slender tubular cross-sections, Engineering Structures 175 (2018) 549–564.

[22] EN 1993-1-1, Eurocode 3: Design of steel structures — Part 1-1: General rules and rules for buildings, European Committee for Standardization, Brussels, Belgium (2005).

[23] A. G. J. Way, M. D. Heywood, Design of light steel sections to Eurocode 3, SCI Electronic Publication: ED005 (Technical Report), The Steel Construction Institute, UK (2012).

[24] C. Kyprianou, P. Kyvelou, L. Gardner, D. A. Nethercot, Characterisation of material and connection behaviour in sheathed cold-formed steel wall systems - Part 2: Analytical modelling, Structures 30 (2021) 1184–1199.

[25] P. Kyvelou, L. Gardner, D. A. Nethercot, Composite action between cold-formed steel beams and wood-based floorboards, International Journal of Structural Stability and Dynamics 15 (8) (2015) 1540029.